# Chapter 2

# Cathodoluminescence Imaging Spectroscopy: A Tool for Investigating Metallic Films and Nanostructures

## 2.1 Introduction

Understanding nanoscale optical phenomena is critical for the future miniaturization of photonic components. Traditional optical probes are limited in resolution by diffraction to dimensions greater than $\lambda/2$. This so-called diffraction limit has been pushed to tens of nanometers using near-field excitation or detection techniques. Unlike photons, electrons are not subject to the diffraction limit of light and can be focused to extremely small spot sizes (<5 nm in a scanning electron microscope, <1 Å in a transmission electron microscope). Thus, electron microscopes are the best tools for obtaining high spatial resolution in excitation. Furthermore, electrons can penetrate through optically thick layers, simultaneously providing information about surface and bulk optical properties [18, 19].

In this chapter, we will show that a combination of scanning electron microscopy (SEM) and cathodoluminescence (CL) imaging spectroscopy can be used to generate propagating surface plasmon polaritons (SPPs) and localized surface plasmons (SPs) on a nanometer scale. We use CL emission from planar metal films fabricated with gratings to determine the propagation distance of near-resonance SPPs. Also, semiconductor nanowires sandwiched between two metal layers illustrate that this technique can be used to excite and image localized surface plasmon resonances.

## 2.2 Cathodoluminescence Imaging Spectroscopy

As we mentioned in Section 1.4, focused electron beam excitation can be used as a tool for investigating plasmonic structures with extremely high spatial resolution and without the requirement of generating and incoupling incident photons. In a transmission electron microscope (TEM), electron energy-loss spectroscopy (EELS) measures the energy loss of inelastically scattered electrons that penetrate through a thin sample, allowing identification of the plasmon resonance. This method has been used to map out SPP dispersion in thin metal films [20, 21] and to determine modes of a number of plasmonic nanostructures such as spheres [22], nanotriangles [23], and nanoholes [24], among others. While the spatial and energy resolution of this technique surpasses many other methods, EELS requires samples to be electron transparent, or to have thickness of <100 nm, impractical for a number of applications.

In contrast, cathodoluminescence spectroscopy measures the emitted *photons* that result from electron beam excitation. The high-energy electrons in a SEM or a TEM impinge on a sample, and the resulting light emission is collected by a mirror located above the sample and sent to detectors. In semiconductors, CL emission is dominated by electron-hole pair excitation and recombination [25]. When the incident beam is scanned across the sample and the resulting light emission is correlated with excitation position, the spatial position of microstructural defects can be determined [26]. We have chosen to use this technique to investigate plasmonic structures in a SEM, which eliminates the constraint on sample thickness. Previously, CL in a TEM was used to image dipole and quadrupole modes of metal nanoparticles [27] and nanoholes [28], and more recently in a SEM to map modes of nanowires [29] and annular nanoresonators [30], whispering-gallery modes in annular grooves [31], and SPP Fabry-Perot resonators [32].

To investigate metallic films and nanostructures using CL here, a 30 keV electron beam from a FEI XL-30 SFEG SEM with a beam diameter of approximately 5 nm irradiates the sample. This beam passes through an aperture in a paraboloidal mirror and scans across the surface of the sample. The outcoupled light is collected by

the mirror with an acceptance angle of ±80° from the surface normal, and through software is correlated with the excitation position. An aluminium waveguide attached to the mirror sends the collected light through a monochromator (set to a central wavelength) and into a photomultiplier tube (PMT) or charge-coupled device (CCD) detector. This is shown schematically in Figure 2.1a.

To measure SPP propagation distance, we excite SPPs at a well-known distance from a nanoscale grating in the metal film. The grating couples the SPPs to free-space photon modes detected in the far field, and the SPP damping is probed by varying the distance between excitation spot and grating (see schematic in Figure 2.2a and 2.2b). Experiments were performed on both Ag and Au films, at frequencies ranging from close to resonance to the near-infrared. The experimentally determined propagation lengths were compared with the values expected for perfectly smooth films, calculated using the optical constants measured on the samples under study.

To perform spectrally resolved CL imaging, such as the results presented in Section 2.4, the position of the scanning electron beam is correlated with the collected light emission. The result is a hyperspectral image of CL emission that varies spatially with excitation position and spectrally with wavelength. Slices in wavelength through this image reveal the regions of most efficient excitation and outcoupling of CL intensity. This, along with CL spectroscopy, is used to characterize Ag-coated ZnO nanowires.

## 2.3 Measuring SPP Propagation Length Near Resonance

As the dielectric constants of plasmonic metals are dispersive, the propagation length of SPPs is strongly frequency dependent, as seen in Figure 2.3 [11]. In the visible and near-infrared, propagation distances as long as 100 μm have been measured for Ag and Au films [33]. Near the surface plasmon resonance frequency, in the UV/visible for Ag and Au, the propagation lengths are much shorter, and it becomes increas-

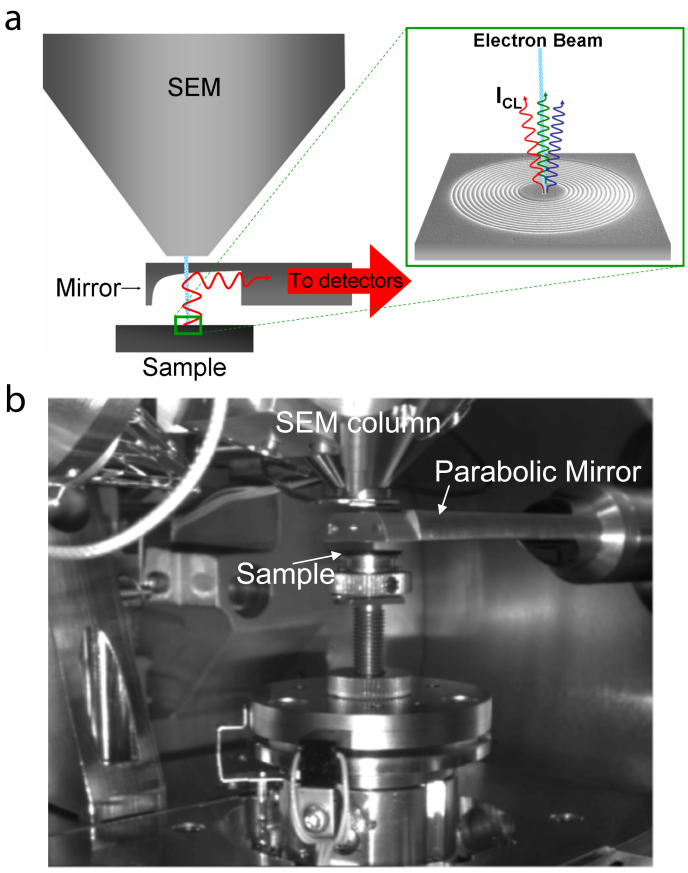


Figure 2.1. (a) Schematic illustration and (b) camera image of cathodoluminescence experimental setup. The electron beam passes through an aperture in a paraboloidal mirror and scans across the surface of the sample. The emitted light is captured by the paraboloidal mirror, sent through a lightguide and into detection optics (grating monochromator, PMT detector, and CCD detector).

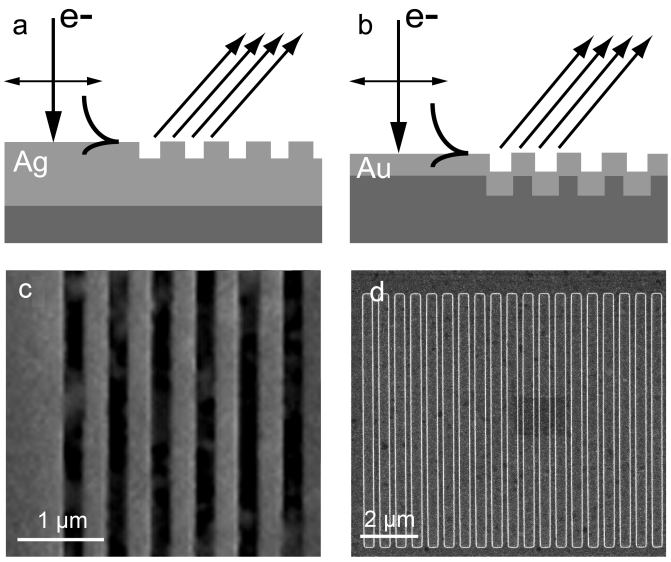


Figure 2.2. Schematic of excitation and outcoupling of surface plasmon polaritons on samples made by (a) FIB milling (Ag) and (b) electron beam lithography (Au). The electron beam is incident normal to the surface of the metal film with varying distance from the grating edge. Far-field radiation from the grating is then collected and analyzed. SEM images of the Ag and Au gratings are shown in (c) and (d), respectively.

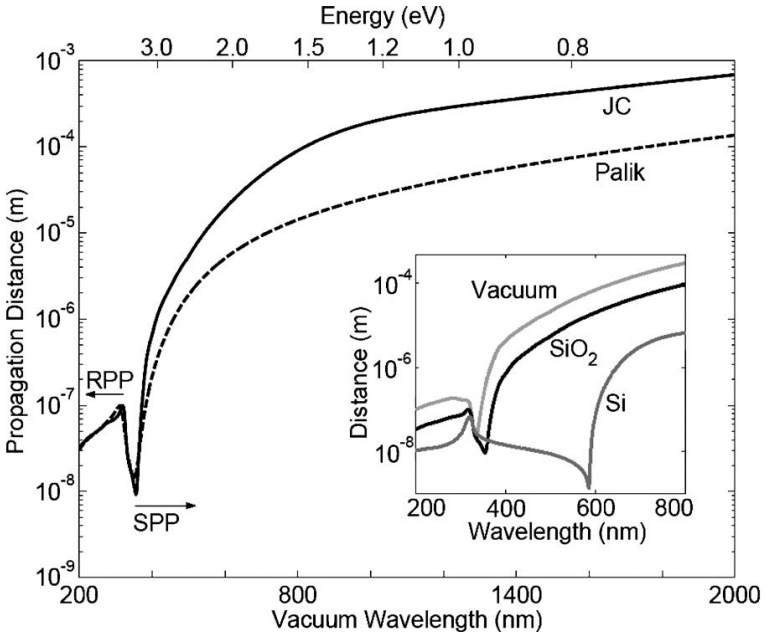


Figure 2.3. SPP propagation length for the $Ag/SiO_2$ geometry calculated using the optical constants of Johnson and Christy [34] (solid) and Palik [35, 36] (dotted). A vanishing propagation length occurs at the surface plasmon resonance, located at $\lambda = 355$ nm (358 nm) for Palik (JC). The local maximum at 320 nm coincides with the transition between quasi-bound (QB) and radiative (RPP) modes. Inset: Comparison of SP propagation for Ag/Air, $Ag/SiO_2$, and Ag/Si geometries plotted about the SP resonance. From [11].

ingly difficult to experimentally determine these distances with conventional optical techniques. Interestingly, it is this frequency range just below the surface plasmon resonance that holds the greatest potential for photonics because the wavelength of the SPPs in this region is much shorter than its free-space counterpart, the group velocity is reduced, and the electric fields are highly concentrated. The near-resonance SPPs therefore have the potential to enable the miniaturization of optoelectronic devices, to control the propagation of optical pulses, and to concentrate light in nanoscale volumes. In light of these applications, it is important to understand the propagation lengths of near-resonance SPPs.

### 2.3.1 Grating Fabrication

Ag and Au films patterned with gratings were fabricated by two different methods. First, a 400 nm thick Ag layer was evaporated onto a quartz substrate. With a focused ion beam (FIB) using a liquid $Ga^+$ source, gratings with 500 nm pitch and a depth of 50 nm were milled in the silver, as illustrated in Figure 2.2a. A second sample was fabricated using electron beam lithography (EBL) to pattern grating structures with a pitch of 500 nm in a poly(methyl methacrylate) (PMMA) layer, spun on a Si wafer. By developing the exposed PMMA and etching the Si in a $SF_6$ plasma, grating structures with an approximate depth of 70 nm were transferred to the Si substrate. An Au film with a thickness of 70 nm was then deposited on the Si by thermal evaporation, shown schematically in Figure 2.2b. Figures 2.2c and 2.2d show top-view SEM images of gratings fabricated with FIB milling and EBL, respectively.

### 2.3.2 CL Measurements

When focusing the electron beam at the edge of a grating, a broad spectrum was observed with a maximum in emitted CL intensity at the surface plasmon resonance. The monochromator was set to several wavelengths above this resonance to compare the CL emission intensity with varying beam position for different photon energies. CL intensity line profiles were either collected by the analysis of two-dimensional images, or using a single line scan.

Figure 2.4a shows the CL intensity collected from the Ag film as a function of distance between the exciting electron beam and the edge of the grating. Data was collected at wavelengths of $\lambda$ = 400, 500, and 600 nm. An exponential decay in intensity is observed as the electron beam moves away from the grating. This intensity decay is slower for longer wavelengths, implying longer SPP propagation lengths at longer wavelengths. CL intensity profiles were also collected on Au films, and are plotted in Figure 2.4b for $\lambda$ = 550 and 600 nm. Signal-to-noise ratios proved to be smaller due to lower signal levels in this case, but similar intensity decays can be discerned at longer wavelengths than for Ag.

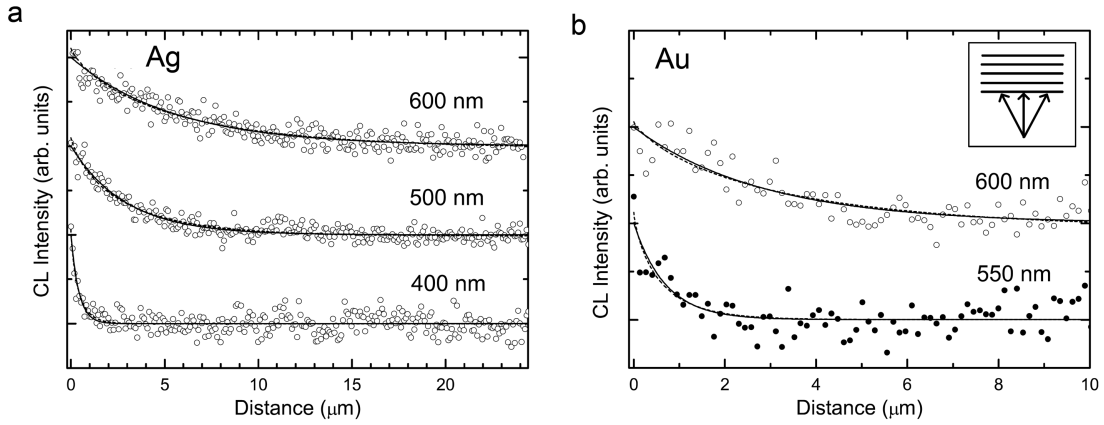


Figure 2.4. Cathodoluminescence intensity (open and closed circles) as a function of distance between the electron beam and grating edge for (a) an Ag film, with profiles collected at $\lambda$=400, 500, and 600 nm, and (b) an Au film, with profiles collected at $\lambda$=550 and 600 nm. A constant background is subtracted from all curves that are then normalized and shifted vertically along the CL intensity axis for clarity. Fits of (2.1) to the data using the angle-dependent grating coupling efficiencies $\alpha(\theta) = \delta(\theta)$ and $\alpha(\theta) = 1/\pi$ are shown as solid and dashed curves, respectively. The two models overlap in these plots in most cases. The inset in (b) schematically demonstrates that the electron beam acts as a point source of SPPs that propagate toward the grating over a broad angular range.

We note that all CL data curves exhibit a significant background intensity that is constant far away from the grating. This may be attributed to radiation from SPPs that couple out from random surface roughness. In order to compare the CL intensity decays for different wavelengths, normalized intensity is plotted in Figure 2.4 after the subtraction of these background values, determined using the fit procedure described below, and the curves are each shifted vertically for clarity.

### 2.3.3 Comparison with Theory

To correlate the CL intensity decays with the exponential decay of SPPs, we note that the electron beam generates SPPs in a point source. After excitation, the SPPs propagate over a large angular range toward the grating (see inset in Figure 2.4b). The measured CL intensity as a function of distance between the excitation spot and the grating edge $x$ is therefore described by

$$I(x) = I_b + I_0 \int_{-\pi/2}^{\pi/2} \alpha(\theta) \mathrm{e}^{\frac{-x}{L_{\mathrm{SPP}} \cos\theta}} d\theta, \tag{2.1}$$

where $I_b$ is the background intensity, $I_0$ is the SPP intensity scattered at the grating edge, $L_{\mathrm{SPP}}$ is the SPP propagation length, and $\alpha(\theta)$ is the angle-dependent grating coupling efficiency. The latter is unknown, but assuming that it is a monotonically decreasing function of $\theta$, we can obtain upper and lower estimated limits to $L_{\mathrm{SPP}}$ from the measured CL intensity profiles using $\alpha(\theta) = 1/\pi$ and $\alpha(\theta) = \delta(\theta)$, respectively, where $\delta$ denotes the Dirac delta function. Both models were fitted to the CL data using nonlinear regression, yielding estimations of $L_{\mathrm{SPP}}$ and the background intensity $I_b$. The latter amounted to typically one to three times $I_0$. The fits to the data displayed in Figure 2.4 are plotted through the data as solid and dashed curves for $\alpha(\theta) = \delta(\theta)$ and $\alpha(\theta) = 1/\pi$, respectively.

Measurements were also performed at other wavelengths, and the fitted upper and lower bounds to $L_{\mathrm{SPP}}$ are shown versus collection wavelength in Figure 2.5. For both Ag (closed symbols) and Au (open symbols), a clear increasing trend is observed as the wavelength increases above resonance. Figure 2.5 also shows the calculated

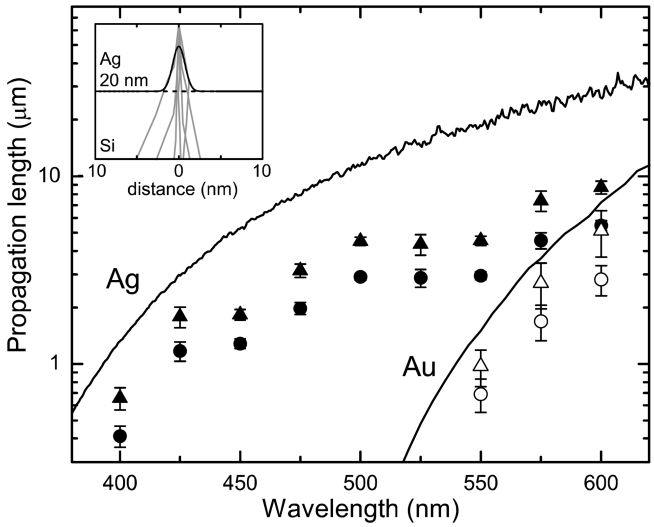


Figure 2.5. SPP propagation lengths $L_{\mathrm{SPP}}$ fitted from CL intensity data as in Figure 2.4 versus wavelength for Ag (closed symbols) and Au (open symbols). The values obtained using $\alpha(\theta) = 1/\pi$ are represented by triangles, and those using $\alpha(\theta) = \delta(\theta)$ by circles. The solid lines are the calculation of SPP propagation lengths for Ag and Au using experimental data for the dielectric constant considering bulk absorption in the film and leakage radiation. The inset shows several 30 keV electron trajectories in a plane at a depth of 20 nm.

propagation lengths as a function of wavelength on perfectly smooth films. For the optically thick Ag film, this value is obtained by considering only bulk absorption losses [3]:

$$L_{\mathrm{SPP}} = (2k_x'')^{-1} = \frac{c}{2\omega}\left[\mathrm{Im}\left(\frac{\varepsilon_m}{1+\varepsilon_m}\right)\right], \tag{2.2}$$

where $k_x''$ is the imaginary part of the SPP wavevector, $\varepsilon_m$ is the complex dielectric function of the metal, $c$ is the speed of light in vacuum, and $w$ is the frequency.

For the 70 nm Au film, in addition to absorption losses, the SPPs propagating at the vacuum/metal interface lose energy due to leakage radiation into the Si substrate. The propagation length including this radiation loss was obtained from the imaginary part of the SPP wave vector calculated by solving the dispersion relation for the vacuum/Au/Si system [37]. For both samples, the propagation lengths are calculated

using experimental values for $\varepsilon_m$ determined from ellipsometry measurements on the metal films used. The surface plasmon resonance wavelengths predicted from these complex dielectric constants are 340 nm for silver and 540 nm for gold.

Irrespective of the functional form of $\alpha(\theta)$, a difference between measured and calculated dampings is observed that may be due to several additional loss processes. One of them is surface roughness of the films [38], which causes in-plane scattering of SPPs and coupling of SPPs to far-field radiation [39]. Additionally, grain boundaries and surface impurities could have a detrimental effect on SPP propagation. The fact that the observed propagation lengths on the Ag sample appear to deviate further from the calculated values than those on the Au sample cold arise from differences in surface morphologies and impurities.

## 2.4 Investigating Semiconductor-Metal Nanostructures Using Cathodoluminescence

Cathodoluminescence imaging spectroscopy has been used for quite some time to correlate microstructural defects in semiconductors with light emission intensity [26]. In this section, we investigate an Ag-coated ZnO nanowire shown schematically in Figure 2.6 using CL. One of the benefits of CL spectroscopy over conventional optical techniques is that an electron beam can penetrate through an optically thick film. We take advantage of this feature here by exciting through the top Ag layer and into the ZnO nanowire, and observing the resulting luminescence.

### 2.4.1 Sample Fabrication

ZnO nanowires approximately 100 nm diameter and 10 μm tall are grown by chemical vapor deposition on a sapphire substrate using Au as the catalyst [40, 41]. After sonication in isopropyl alcohol (IPA), nanowires are dropcast onto a Si substrate coated with 100 nm Ag. A second Ag layer 100 nm thick is evaporated, with the longitudinal cross section shown schematically in Figure 2.6a. To create shorter nanowires, the

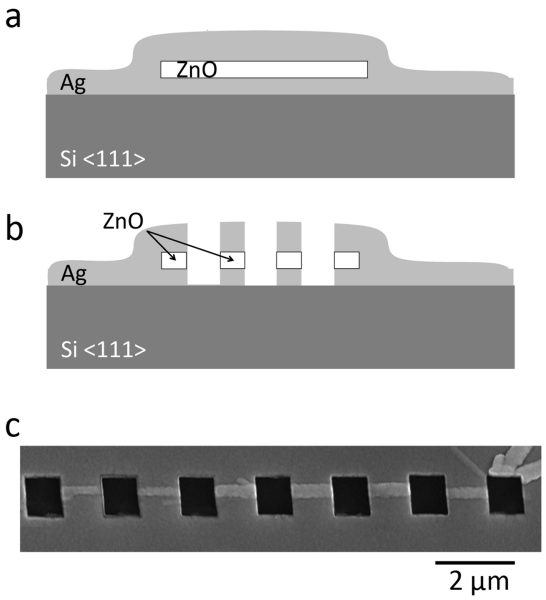


Figure 2.6. (a) Schematic cross section of a ZnO nanowire dropcast on an Ag film, and then overcoated with Ag. (b) Shorter resonators are created by cutting the wire into segments using a FIB. (c) Top-view SEM image of the Ag-coated ZnO nanowire after FIB cutting.

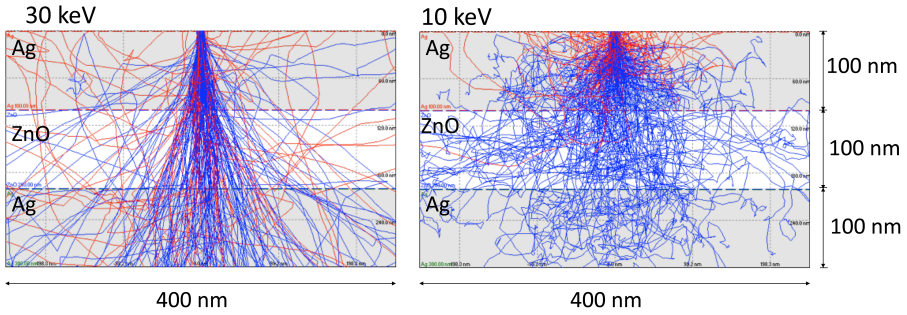


Figure 2.7. Monte Carlo simulation of electron trajectories [42] in a 4-layer system consisting of Ag/ZnO/Ag (each 100 nm thick) on Si for an incident electron beam with 5 nm diameter at (a) 10 keV and (b) 30 keV.

coated NW is cut with a FIB to segments approximately 1 μm long (Figures 2.6b and 2.6c). After measurements, an additional layer of 20 nm Cr is thermally evaporated over the sample to damp surface plasmons on the outer Ag/air interface, and CL measurements are repeated.

### 2.4.2 CL Spectroscopy and Imaging

Unlike for the grating structure studied in Section 2.3, the electron beam excitation conditions for the Ag-coated ZnO nanowires is optimized for maximum interaction volume in the semiconductor. As a result, the spatial resolution is degraded. This is illustrated in the Monte Carlo simulation of electron trajectories [42] in Figure 2.7. Here, we consider a 4-layer system of Ag/ZnO/Ag (each 100 nm thick) on a Si substrate. For excitation at 30 keV, the same condition used to investigate the metal gratings, the initial spotsize of 5 nm broadens to approximately 50 nm in the ZnO layer. If we instead consider a lower incident beam energy of 10 keV, the interaction volume is now confined mostly within the ZnO layer, although with a poorly defined spot size in the semiconductor of approximately 200 nm. This demonstrates that we can sacrifice spatial resolution in excitation to obtain more interaction of the incident electrons in the ZnO layer.

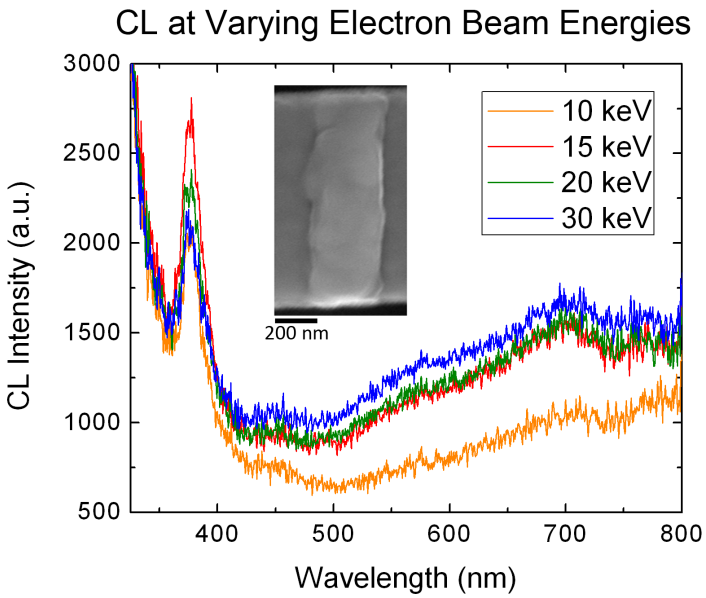


Figure 2.8. CL spectra of an Ag-coated ZnO nanowire for incident electron beam energies of 10, 15, 20, and 30 keV. Maximum emission intensity at the bandedge ($\lambda$ = 375 nm) is seen for excitation at 15 keV. Inset: Top-view SEM image of the nanowire.

The excitation conditions are optimized for maximum CL intensity at the ZnO bandedge ($E_g$ = 3.3 eV, or $\lambda$ = 375 nm). CL spectra at incident beam energies of 10, 15, 20, and 30 keV are shown in Figure 2.8. These spectra are 20 s acquisitions with the CCD detector while the electron beam is scanned quickly over the area shown in the SEM inset. Brightest CL emission at the band-edge is seen for excitation at 15 keV. Other spectral features at shorter wavelengths are due to SPs outcoupling from the rough Ag film, and features at longer wavelengths are most likely due to cavity resonances inside the ZnO nanowire.

We also collect a series of images that map CL emission intensity spatially as a function of excitation position and spectrally versus wavelength. Figure 2.9a is an SEM image of an Ag-coated ZnO nanowire, showing the region scanned for the CL spectrum imagng. The CL images in Figure 2.9b are acquired by scanning the electron beam across the region in the SEM image to form an image of 80 $\times$ 26 pixels$^2$, with a per pixel dwell time of 1 s and spatial resolution of 15 nm/pixel. The CCD

acquires a spectrum at each pixel, and slices through this hyperspectral image reveal the images in Figure 2.9b at the indicated wavelengths ($\lambda$ = 350, 375, 500, 600, and 700 nm), with a 20 nm spectral passband. This acquisition takes approximately 1 hr, during which time the program also corrects for spatial drift every 15 pixels. Bright yellow regions in the images correspond to positions where electron excitation results in bright CL emission. At $\lambda$ = 350 nm, very near the SP resonance for Ag/air, bright emission occurs fairly uniformly for excitation along the wire. This is expected, as SPs excited near resonance will outcouple due to surface roughness after propagating only a very short distance.

At the ZnO bandedge ($\lambda$ = 375 nm), bright emission is seen for excitation near the left end of the wire. Collection asymmetry by the mirror was eliminated as a contributing factor by rotating the sample 180° and seeing similar behavior. This asymmetry of emission fro the ZnO could be due to several factors. Most likely, the FIB process resulted in the left end of the nanowire having less Ag coating, resulting in brighter emission. The emission at $\lambda$ = 500 nm shows several peaks in intensity along the wire, which may be due to either a standing resonance of the ZnO core or of the outer Ag/air interface. Similar features are observed at $\lambda$ = 600 nm. At $\lambda$ = 700 nm, bright emission is only seen for excitation at the left end of the wire. Emission from ZnO in the band of $\lambda$ = 600–800 nm can be attributed to defect luminescence.

After measurements were completed, the sample was coated with a 20 nm thick Cr layer to differentiate between emission from the outer Ag/air interface and modes of the ZnO nanowire. We then repeated CL measurements on the same nanowire. The resulting CL images are seen in Figure 2.9c. These images were acquired as $51\times8$ pixels$^2$ (spatial resolution 22 nm/pixel), with a 10 s dwell per pixel and no drift correction. Because the spatial area scanned was smaller than before coating with Cr, the unscanned area is shown in blue. Also, significant drift did occur during the collection that can be identified in the images.

As expected, at $\lambda$ = 350 nm, near the SP resonance, emission from SPs at the Ag/air interface has been quenched. Band-edge emission at $\lambda$ = 375 nm in the Cr-

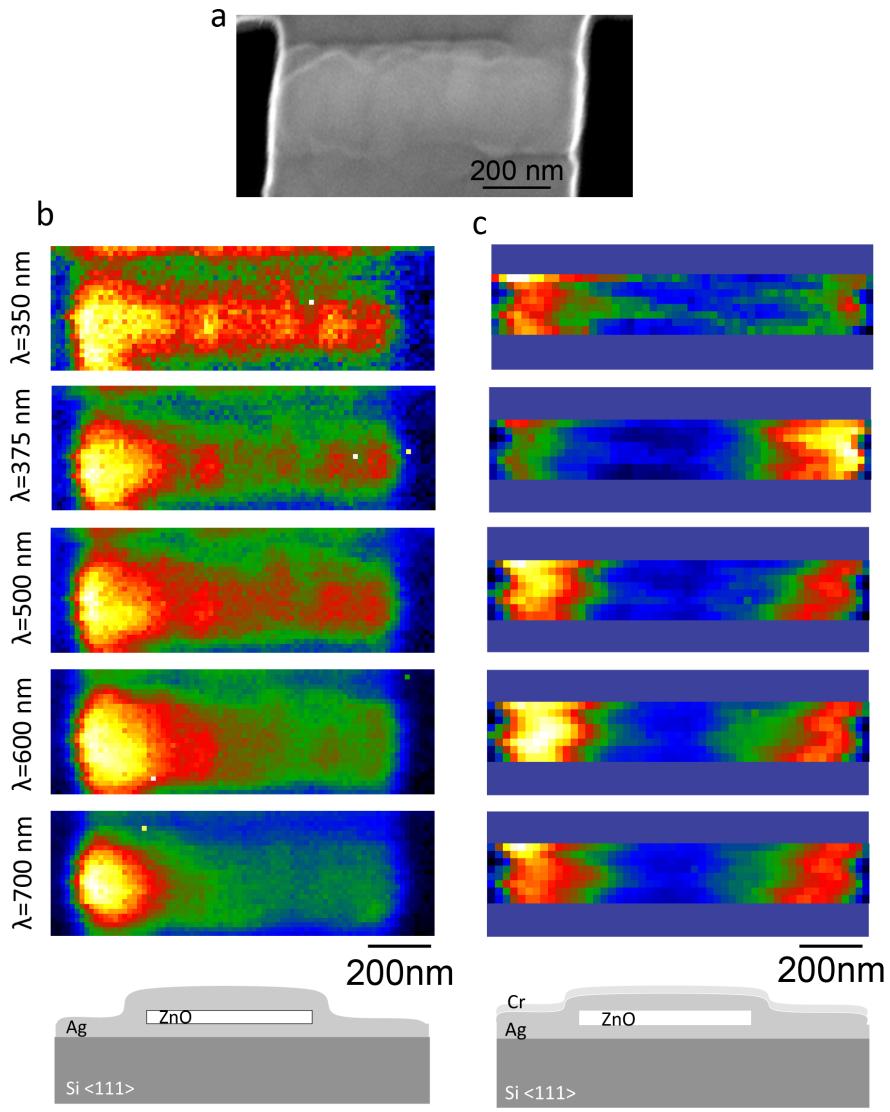


Figure 2.9. (a) SEM image of a FIB cut Ag-coated ZnO nanowire. (b) CL images at the indicated wavelengths of the nanowire shown in (a). (c) CL images at the indicated wavelengths of the nanowire coated with a thin layer of Cr, which damps SP propagation on the outer interface. Dark blue outline compensates for smaller scan region in Cr-coated images. In all images, yellow regions illustrate positions where electron beam excitation results in bright CL emission.

coated nanowire is now brightest for excitation at the right end of the nanowire. At the longer wavelengths ($\lambda$ = 500 nm and $\lambda$ = 600 nm), where previously bright regions were observed for excitation along the length of the wire, the Cr coating has also quenched this emission. Thus, we can conclude that the source of emission in the Ag-coated ZnO nanowire without Ag was due to a SP mode of the outer Ag/air interface, and not of the interior nanowire. Even in the Cr coated structure, emission in the defect luminescence band is concentrated at the left end of the nanowire.

## 2.5 Chapter Summary

These results show that CL imaging spectroscopy is a useful tool for high-resolution characterization of plasmonic nanostructures. It can be applied to study the propagation and damping in a wide array of geometries, including plasmonic waveguides, tapers and cavities. The ultimate resolution of this CL imaging technique is determined by the excitation volume in the metal film: thinner metal films will yield higher resolution. As an example, the inset in Figure 2.5 shows trajectories of 30 keV incident electrons on a 20 nm thick Ag film on Si calculated using a Monte Carlo simulation program [42]. It shows the angular spread of the electron beam in a 20 nm thick film is only a few nanometers, and thus in such a geometry the lateral resolution is mostly determined by the incident beam diameter. More detailed calculations of the generation of SPP surface waves by the electron cascade inside the film are required to study the ultimate resolution that can be achieved.

We have determined the propagation length of surface plasmons near the surface plasmon resonance for both Ag and Au films. Propagation lengths as short as several hundred nanometers are determined, and the propagation length increases as the wavelength is increased above resonance. Comparing these results with calculations accounting for loss due to absorption in the film and to leakage radiation shows that other loss mechanisms appear to have a large contribution as well.

We also investigated Ag-coated ZnO nanowires using this technique and demonstrated that electron beam excitation can be localized in depth to most efficiently

excite luminescence from the ZnO NW core. Spectrally resolved CL images demonstrate that surface plasmons on the outer Ag/air interface emit brightly near the SP resonance and form standing resonances at longer wavelengths. Coating the wire with a thin layer of Cr quenches this luminescence, but not the band-edge or defect-band luminescence from the ZnO core. The ultimate imaging resolution of this technique will be determined by the excitation volume of SPPs by electrons, which may enable the characterization of SPPs and localized modes in a large array of plasmonic nanostructures.